Ellipsometry and spectroscopy on 1.55 μm emitting Ge islands in Si for photonic applications

V. M. Lavchiev,[1,*] U. Schade,[2] G. Hesser,[3] G. Chen,[4,*] and W. Jantsch[4]

[1]*Institute for Microelectronics and Microsensors, Johannes Kepler University, Altenbergerstrasse 69, 4040 Linz, Austria*

[2]*Helmholtz-Zentrum Berlin für Materialien und Energie, Albert-Einstein-Strasse 15, 12489 Berlin, Germany*

[3]*Zentrum für Oberflächen und Nanoanalytik (ZONA), Johannes Kepler Universität, Altenbergerstrasse 69, 4040 Linz, Austria*

[4]*Institute for Semiconductor and Solid State Physics, Johannes Kepler University, Altenbergerstrasse 69, 4040 Linz, Austria*

(Received 23 February 2012; revised manuscript received 1 July 2012; published 13 September 2012; publisher error corrected 29 May 2013)

Single-layer and mutlilayer Ge islands in a Si matrix, grown by solid source molecular beam epitaxy (MBE) on Si and SOI substrates in a self-assembled mode, are investigated by means of optical spectroscopy and spectroscopic ellipsometry in the spectral range of 0.54–4.5 eV. This range widely encloses the characteristic optical transitions of the islands around 1.5 μm, that is, 0.82 eV. By introducing and developing an appropriate model, the technique enabled determination of the dielectric constants and the film thicknesses of the structure. Knowledge of these constants is crucial for the potential applications of Ge nanostructures for photonic and optoelectronic devices. Moreover, the technique allowed observation of the transition resonances of the Ge dots and the Ge wetting layer. The two methods are implemented as a joint tool to investigate the behavior and properties of the Si/Ge nanostructures in the near infrared spectral range.

DOI: 10.1103/PhysRevB.86.125421 PACS number(s): 81.07.Ta, 78.67.−n

I. INTRODUCTION

Incorporation of Ge nanostructures into Si has been an area of intense research in the past few years in view of not only studying fundamental problems (e.g., strain and surface phenomena in Si/Ge structures, valence and conduction band modifications, carrier mobility, strain and morphology evolution, etc.[1–3]), but also in view of possible applications. Control has been achieved with respect to the thickness of the individual Si or Ge layers and monolayers,[4–6] to the positions of the Ge islands,[4,7–9] their shape (e.g., dome- or pyramidlike),[10,11] strain in the layers (tensile or compressive),[12,13] their crystallographic orientation, their optical[14–16] and electrical[17,18] properties, etc. The engineering of the structural and electro-optical properties of materials, and more specifically of SiGe, has various applications in optoelectronics such as developing of optoelectronic components,[19–21] photonic structures like optical waveguides (WGs), photonic crystals, cavities, etc.[22–25]

For modeling and designing photonic structures for the next generation devices, the complex dielectric function (DF) $\tilde{\varepsilon} = \varepsilon_r + i \cdot \varepsilon_i$ [or equivalently, the refractive index n and extinction coefficient κ, $\sqrt{\tilde{\varepsilon}} = (n + i \cdot \kappa) = \tilde{n}$] has to be known with good accuracy. One of the most efficient techniques for finding $\tilde{\varepsilon}$ of a layered medium is spectroscopic ellipsometry (SE).[26,27] The measured values are represented by Ψ and Δ related to the complex Fresnel coefficients $\tilde{R}_p$ and $\tilde{R}_s$, of the p- and s-polarized light beams, respectively, by $\tilde{\rho} = \tilde{R}_p/\tilde{R}_s = \tan(\Psi)e^{i\Delta}$. Ψ and Δ are proportional to the angle P between the polarizer axis and the plane of incidence. The high accuracy of the technique is based on obtaining two parameters simultaneously (Ψ and Δ) at different incident angles θ_{inc} and wavelengths λ_{inc} and allows its application for precise measurements of quantum dots (QDs). At the same time, its limitation to structures with feature size comparable to or smaller than λ_{inc}, and a roughness of maximum 10% of λ_{inc} constitute an operational domain, well suited to the range of interest for films containing Ge islands.

Profound ellipsometry studies of Ge islands have already been conducted.[28–30] However, the optical communication wavelength of 1.5 μm has not been covered yet in any SE experiments up to date. The lack of data about the optical constants of Si/Ge nanostructures hampers their integration into optoelectronic and photonic devices in the spectral range where the luminescence of the dots resides, which is one of the most important properties of these structures. The parameters, obtained by SE, can be applied particularly for simulations related to design and optimization of different devices. Such simulations are used by many groups,[22–25] but without treatment of the problem of the dielectric constants.

In the present study, (i) SE is carried out in the spectral range where the optical transitions of the Ge islands occur. Thus, we not only extend the range of the measurements below the wavelength of 1.5 μm, but we also develop a model for Ge islands which gives almost perfect agreement with the experiments permitting extraction of the film thicknesses, their refractive indices, and extinction coefficients. (ii) Moreover, this technique enabled observation of the Ge dots optical resonances which has not been demonstrated prior to this work. This observation permits a direct treatment of the dielectric function and the energy band gap of Si/Ge nanostructures.

The technique can be combined with photonic simulations within the beam propagation method (BPM) to optimize the optoelectronic components of single-platform devices. The combination of these two methods has been used to design optically active rib WGs and photodetectors from Si with embedded Ge islands.[31,32] Design and optimization of the devices were performed in three stages: (i) optical spectroscopy to investigate the optical transitions in the Si/Ge structure; (ii) SE to determine the sample's optical constants; and (iii) use of n and κ extracted from ellipsometry as input parameters in the BPM simulation code.

II. EXPERIMENT

In our ellipsometry experiments, two types of samples have been investigated. To extract the optical constants of

 ©2012 American Physical Society

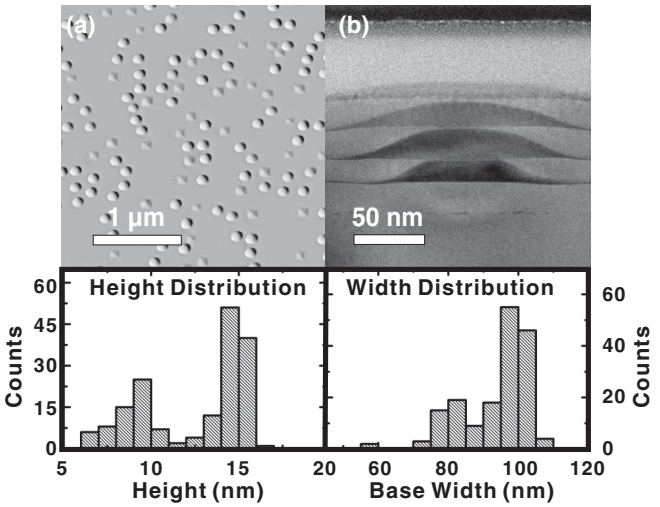

FIG. 1. (a) SEM image of self-assembled Ge islands in Si; the capping layer is omitted on this sample for demonstration purposes; and (b) TEM image of a stack of Ge islands.

the films, a sample with a single layer of self-organized Ge islands grown on Si substrate was used. Samples with a stack of self-organized Ge dots have been also measured. Although a multilayer structure had been expected to provide stronger signals and allowed observation of the resonances in the Ge islands, this could, however, complicate the evaluation, for example, due to the interference resulting from the layers and a more complex fitting model would be necessary.

Si/Ge structures were grown by solid source Riber SIVA 45 molecular beam epitaxy (MBE) either on a Si or on a SOI substrate. The sample with a single layer of self-organized Ge dots was prepared as follows: Before the Ge growth, a Si buffer layer is grown on the 1 mm thick Si substrate for improving the quality of the substrate. The buffer layer is grown at a temperature of $T_b = 550\,^{\circ}\mathrm{C}$, to a thickness of 25 nm at a rate of 0.5 Å/s. After that, a single layer of Ge dots was deposited as nominally 6 monolayers (ML) of Ge grown at $T_i = 650\,^{\circ}\mathrm{C}$ and a repetition rate of 0.05 Å/s. Finally, a capping layer of 115 nm Si deposited at a temperature of $T_c = 700\,^{\circ}\mathrm{C}$ and rate of 1 Å/s was grown. This procedure produced Ge islands of self-assembled type shown in Fig. 1(a). The samples with stacks of islands have been manufactured in a similar procedure described above, but the Si buffer, the Si spacer (between the alternative Ge QDs layers), and the Si capping layers have been fixed to a thickness of 45, 15, and 2 nm, respectively. Figure 1(b) shows a TEM image of a stack of Ge islands. Also shown in Fig. 1 is statistics on size distribution of the Ge dots. It is derived from a $3.5 \times 3.5\ \mu\mathrm{m}$ region and demonstrates the broad dispersion of both the height and the width of the Ge dots. A typical phenomenon in the multilayer growth of Ge dots is the relative conservation of this distribution accompanied by a change of the dot size—increase in width and decrease in height. Such size distribution is typical for the self-assembled samples. Thus, the results presented in this work are restricted to Ge dots with such a size spreading.

III. RESULTS AND DISCUSSION

In the first step the samples were investigated by optical spectroscopy which revealed near infrared photoluminescence (PL) of Ge islands at a wavelength $\lambda = 1500$ nm, right at the most popular telecom band.[15,32] The PL spectra allowed us to define the spectral range for the SE investigations and further on for the photonic simulations. Figure 2(a) shows the PL spectrum of the Ge dots at different temperatures. The measurement is performed on a grating spectrometer (SPEX) setup by the lock-in technique. Ar^+ laser ($\lambda = 488$ nm) was used as an excitation source and liquid-N_2-cooled Ge detector for detection of the signal. Detection of the PL in wider spectral range is limited by the sensitivity of the Ge detector (0.73–1.77 eV). Decrease of the signal intensity with the temperature increase can be seen, which is expected because in this type of nanostructures the nonradiative processes compete strongly with the radiative transitions at elevated temperatures.

The graph shows several optical transitions. The transitions observed in the range ~0.75–0.9 eV are assigned to the Ge dots. The wide spectral distribution of these transitions is due to the size inhomogeneity of the dots. The signal in the range ~0.9–1.0 eV is assigned to the Ge wetting layer which performs much like a quantum well. Finally, the peaks at ~1.03–1.14 eV represent the nonphonon and phonon-assisted (optical and acoustic) transitions in Si. The inset in Fig. 2(a) illustrates schematically a theoretical model of how the optical transitions in Ge dots occur: The growth of Ge on Si, with lattice constants $a_{Ge} = 5.65$ Å and $a_{Si} = 5.63$ Å, causes lattice mismatch and strain modification of the energy bands of the Ge/Si system. This energy band modification results particularly in that the electron from the excited electron-hole pair in Ge dot resides in the energetically more favorable state

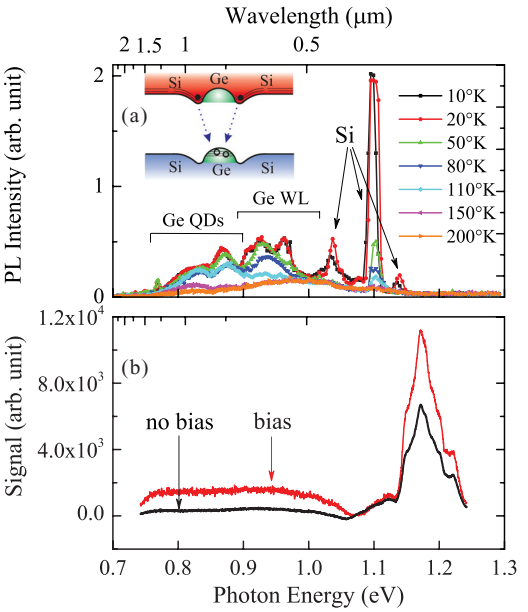

FIG. 2. (Color online) (a) Photoluminescence spectra of a Ge dot sample. Indicated are the PL transitions from the Ge dots, from the Ge wetting layer (WL) and the phonon transitions in Si at different temperatures. Excitation: Ar+ laser, $\lambda = 488$ nm. (b) Photoresponse of a Ge dots based infrared photodetector.

in the neighborhood Si; the hole remains in the Ge dot. In the recombination process, the electron moves back to the Ge dot.

To study the photoresponse of the Ge dots and, in general, their applicability as an active medium for light detection in the NIR range, a vertical pin junction with Ge dots was grown (similar to Ref. 12). The pin diode structure was prepared on an SOI substrate. The MBE growth sequence is as follows: A 100-nm-thick B-doped Si buffer layer with an acceptor concentration of 5×10^{18} cm^{-3} forms the p channel of the junction. Then a 30 nm intrinsic Si buffer was deposited followed by several layers of Ge islands (7 monolayers Ge) deposited at 650 °C. At this coverage, Ge islands conglomerate at the pits. After each Ge layer there is a 25-nm-thick strained Si spacer layer. On the top, Sb-doped 50-nm-thick Si layer with a donor concentration of 5×10^{18} cm^{-3} and 10-nm-thick Si layer with a concentration of 5×10^{19} cm^{-3} form the n-type channel. The whole stack is structured as a waveguide and the probe light is sent along the waveguide. By this pin configuration, we can achieve (i) thin intrinsic layers (i.e., faster device) and (ii) long light propagation path (i.e., more efficient light absorption). Figure 2(b) demonstrates the photoresponse of the device. The measurement was performed at room temperature with a Fourier spectrometer DA8.22 employing InSb photodetector. The signal is corrected to the photodetector sensitivity and to the light source intensity spectrum (quartz broadband lamp). The offset between the broad peak in the spectral diapason 1.06–1.25 eV in Fig. 2(b) and the phonon and nonphonon peaks in Si in Fig. 2(a) is due to the Stokes shift. Although the behavior of the device around the photon energy 1.06 eV is not fully understood and is a topic outside of the scope of the present work, the operation in the spectral range 0.75–1.25 eV is obvious.

Further on, spectroscopic ellipsometry is performed on such samples. In Fig. 3 experimental data of SE, performed at room temperature, are shown for Ge islands on a Si substrate. Measurements have been performed on a J. A. Woollam VASE ellipsometer. The curves represent the measured values for Ψ and Δ at three different angles of incidence of the probing beam—at 62°, 68°, and 74°. Measurements at different angles increase the reliability of the fit.

As a next step, a multilayer model had to be defined and introduced into the modeling software. The software employs a Levenberg-Marquardt algorithm for numerical solution of the equations describing the model of each layer. Alternatively, Matlab can be used for such numerical solutions by writing our own code. The layer structure and layer sequence are introduced into the model according to the parameters known from the growth procedure. Each layer is described by a complex dielectric function in the spectral range investigated. The dielectric function is specific for each layer and can be described by a set of adjustable parameters. In the fitting procedure we vary (i) the thickness of the layers, (ii) the parameters for the DF of each layer, and (iii) the composition of the mixed layers minimizing deviations of the model from the experimental data for the whole layer stack.

The SE data represent the optical response of the entire layer structure. The experimental values and the fitting in Fig. 3 thus depict the dielectric function of the whole multilayer system, that is, the effective DF of the whole stack (pseudodielectric function). All the layer thicknesses are obtained from the fitting

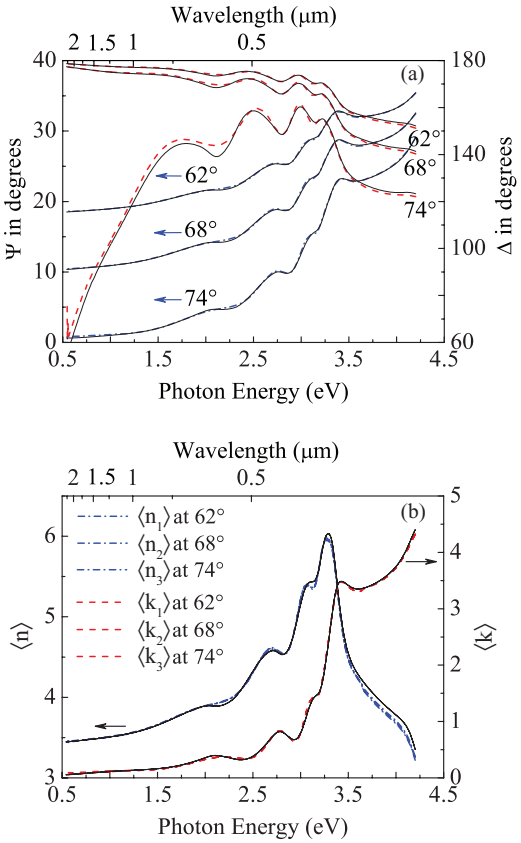

FIG. 3. (Color online) (a) Experimental values for Ψ (dashed-dotted lines) and Δ (dashed lines) for Ge islands grown on Si substrate and the fitting results (solid lines). (b) Experimental and fitting results on pseudorefractive index $\langle n \rangle$ and the pseudoextinction coefficient $\langle \kappa \rangle$.

algorithm except for the thickness of the substrate which was set as fixed. Figure 3(b) shows the fitting curves and the experimental data in terms of a pseudorefractive index $\langle n \rangle$ and a pseudoextinction coefficient $\langle \kappa \rangle$. The pseudodielectric function $\langle \varepsilon \rangle = \sin^2 \theta_{\text{inc}}[1 + \tan^2 \theta_{\text{inc}}(\frac{1-\rho}{1+\rho})^2]$ is derived from the ratio $\tilde{R}_P / \tilde{R}_S$ for the two-layer system air/SiGe by applying Fresnel equations after setting $\varepsilon_{\text{air}} = 1$.

Table I illustrates the multilayer model along with the obtained parameters for the complex dielectric function and thicknesses of the layers.

The model follows the growth sequence of the structure. Layer numbered 0 is the Si substrate and layer 1 is the Si buffer layer. The thickness of the Si buffer is fitted on a preliminary step and further kept fixed. The optical constants of the Si buffer layer have been assumed equal to that of the Si substrate expecting monocrystal formation by the two. Layer 2 is the Ge wetting layer (WL), assumed as an alloy of Ge and Si. This intermixing of Si and Ge happens naturally due to the interdiffusion of the two materials during the high temperature growth (650 °C). The Ge WL is modeled within the parametric semiconductor model.[33] A strong correlation between the thickness of the Ge WL and the composition of the Ge dot layer has been found. This correlation causes the unphysical error of over 100% concentration of one of the two components of the Ge QD layer (the layer composition is discussed below)

TABLE I. Fitting results for the complex refractive index and thickness (in nm) of the layers. The values are shown for the particular energy of interest 0.82 eV.

Layer	Material	Thickness (nm)	Re($\tilde{n}$)	Im($\tilde{n}$)
5	SiO_x layer	$3.76 \pm 1.15 \times 10^{-2}$	≈ 1.45	0
4	Si capping layer	105.9 ± 0.35	≈ 3.48	0
3	Ge Islands layer	1.15 ± 0.47	≈ 3.47	25.46×10^{-4}
2	Ge wetting layer	0.26	≈ 4.26	0.057
1	Si buffer layer	25	≈ 3.48	0
0	Si	1 mm	≈ 3.48	0

and transgressing appropriate 90% confidence limits in the thickness of the Ge dot layer. To avoid this, the thickness of the Ge WL and its optical constants have been fitted at two fitting steps maintaining constant the former or the latter at the different steps. The figure of merit of the fit has been the confidence limit and the difference between the experiment and the fit along with reported thicknesses of Ge wetting layers from the literature. The dielectric function within the parametric model is of a form

$$\varepsilon(\hbar\omega) = \varepsilon_1 + i\varepsilon_2 = 1 + i\sum_{0}^{n}\int_{E_{\min}}^{E_{\max}} S_j(x)\Phi_j(\hbar\omega,x,\sigma_j)dx + \sum_{n+1}^{n+1+p}\frac{A_j}{(h\omega)^2 - E_j^2}. \quad (1)$$

It represents summation over an oscillator ensemble within the measured spectral range ($E_{\min}$, $E_{\max}$) and summation over oscillators outside the measured spectrum. $\Phi(\hbar\omega,x)$ is the broadening function which describes the Gaussian or the Lorentzian broadening associated with the jth oscillators. In the current modeling, Gaussian broadening is assumed:

$$\Phi_j(\hbar\omega,E,\sigma_j) = \int_0^\infty e^{i(\hbar\omega - E + i2\sigma_j^2 s)s}ds - \int_0^\infty e^{i(\hbar\omega + E + i2\sigma_j^2 s)s}ds. \quad (2)$$

$W(x) = f(E)$ is the unbroadened absorption spectrum, which contains also the joint density of states. This function is constructed of n bounded polynomials grouped in ensemble of four (each critical point CP or oscillator is defined by four polynomials):

$$S_j(E) = \sum_{k=0}^{N} p_{j,k}E^k u(E - a_j)u(b_j - E), \quad (3)$$

where $p_{j,k}$ is the polynomial coefficients, a_j, b_j is the bounding energies for the jth polynomial, N is the polynomial order, and $u(x)$ is the Heaviside unit step function.

The characteristic parameters for each CP is the CP energy E, center amplitude A, broadening σ, lower and upper bounding energies E_L and E_U, lower and upper midamplitudes A_L and A_U, and the lower and upper second order polynomial factors L_{2nd} and U_{2nd}.

The oscillators and their parameters, used and obtained within the Ge parametric semiconductor model, are listed in Table II.

Note, that oscillators number 0 and 8 are not active: Oscillator 0 is shown only for consistency of the table and oscillator 8, although not active, is connected with oscillator 7. This means that the data are sensitive to this parameter and oscillator 8 can affect the absorption tail of the dielectric function of the layer. The fitting procedure "shifts" the CPs 2, 6, and 7 outside of the measured range. However, they are connected to the other critical points via the bound polynomials. Thus, these CPs contribute to the model absorption and ensure smooth behavior of $\tilde{\varepsilon}_2$ and via the Kramers-Kronig relations of $\tilde{\varepsilon}_1$. Otherwise, abrupt and unphysical features can be expected at the boundaries of the available ellipsometry data. Figure 4 demonstrates the dielectric function of the Ge WL found through the parametric semiconductor model—the total function ε and its fitting resonances (for more details on parametric semiconductor model, see Appendix A).

TABLE II. Critical point and their characteristic parameters for the dielectric function of the Ge wetting layer.

						Left of CP			Right of CP		
No.	Energy	Amp.	Connect	σ	Discont.	Mid Pos.	Mid Amp.	Second order	Mid Pos.	Mid Amp.	Second order
0	0.6650	0.0000	0, 0	20.000	0.0000	0.5000	0.5000	0.0	0.5000	0.5000	0.0
1	0.8148	0.5939	1, 2	9.543	0.0000	0.5000	0.5000	0.0	0.5000	0.1498	0.0
2	0.0100	0.0010	0, 5	74.911	0.1231	0.9208	0.1691	1.0	0.6107	0.2189	0.0
3	2.7190	14.4132	1, 5	50.610	0.1372	0.1218	0.0228	0.0	0.3519	0.3799	0.0
4	3.1067	8.0317	4, 5	229.714	0.0000	0.5000	0.5000	0.0	0.1497	0.2843	0.0
5	4.3693	31.1631	4, 7	94.287	−0.3247	0.8951	0.7064	1.0	0.6157	0.2624	1.0
6	5.7362	5.1815	5, 7	212.586	0.0000	0.0540	0.0131	0.0	0.9500	0.4952	0.0
7	6.5000	4.1567	5, 7	200.000	0.0000	0.5000	0.5000	0.0	0.5000	0.5000	0.0
8	4.3464	3.0200	8, 7	42.921	0.0000	0.5000	0.5000	0.0	0.9500	0.0010	0.0

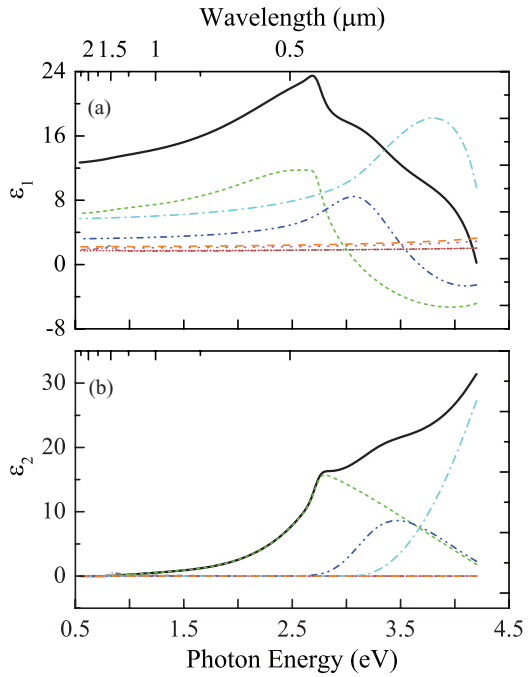

FIG. 4. (Color online) The total dielectric function of Ge wetting layer obtained through the parametric semiconductor model and its oscillators.

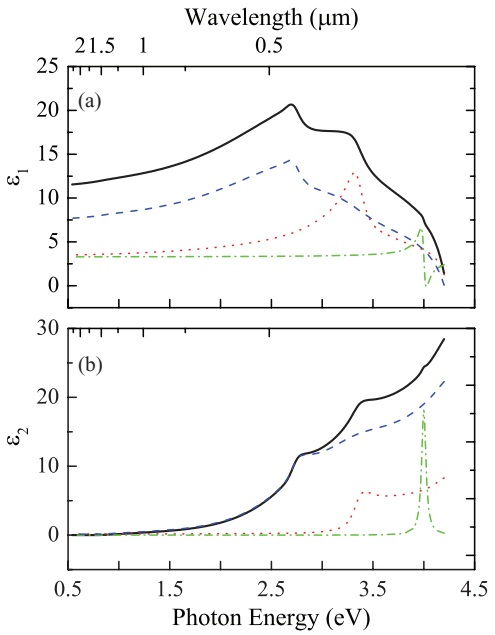

FIG. 5. (Color online) The total dielectric function of Ge dot layer obtained through the EMA model and its three components.

Layer 3 is the Ge island layer. Theoretically, the Ge island layer is represented through the *effective medium approximation* (EMA)[34] describing Ge islands surrounded by a Si matrix. The effective DF of the layer is expressed through the DF of Si (the host) and Ge. The Si portion of the layer is modeled as a parametric semiconductor Si component. The optical parameters of this component are found from the fitting but differ little from that from the literature (thus not discussed here). The Ge portion is modeled by the so-called *complex dielectric additive* (CDA) *layer*—a sum of Lorentzian oscillators added to the dielectric function of Ge found from the parametric semiconductor model (above): $f_{\mathrm{Si}}\frac{\tilde{\varepsilon}_{\mathrm{Si}}-\tilde{\varepsilon}}{\tilde{\varepsilon}_{\mathrm{Si}}+2\tilde{\varepsilon}} + f_{\mathrm{CDA}}\frac{\tilde{\varepsilon}_{\mathrm{CDA}}-\tilde{\varepsilon}}{\tilde{\varepsilon}_{\mathrm{CDA}}+2\tilde{\varepsilon}} = 0$. In this expression f_{Si} and f_{CDA} are the volume fractions of the materials. The linear EMA type of the form $\tilde{\varepsilon} = f_{\mathrm{Si}} \cdot \tilde{\varepsilon}_{\mathrm{Si}} + f_{\mathrm{CDA}} \cdot \tilde{\varepsilon}_{\mathrm{CDA}}$ has been checked in the fitting procedure. We found that it increases the fitting error in comparison to the Bruggeman EMA: It causes huge 90% confidence limit in the thickness of the Ge QDs layer (on the order 1.07 $\pm$1.26 nm) and the composition of the EMA layer (on the order of 88.1 $\pm$ 99.17%). Trying to stay as close as possible to an appropriate confidence limit, a two-component Bruggeman EMA type has been implemented. In addition, it looks like a closer to the physical reality model. The best values from the fitting algorithm (in terms of minimal correlation values in the correlation matrix and appropriate 90% confidence limits) are presented in Table I along with 86.1 $\pm$ 39.65% of CDA (i.e., Ge). Figure 5 demonstrates the total dielectric function of the Ge QDs layer and its fitting components. The fitting components are (i) a Lorentzian oscillator situated at energy $E = 4$ eV, (ii) parametric semiconductor function for the Ge portion of the layer, and (iii) parametric semiconductor function for the Si matrix portion of the layer. In this graph, the Ge and Si parametric functions are found through a similar procedure described for the Ge WL (Fig. 4), but the resonances of these functions are not shown in order to avoid overloading the graph.

Finally, layer 4 is the capping Si layer with a native oxide SiOx atop. The Si capping is modeled within the parametric model for Si with the thickness as a fitting parameter and the optical constants equal to the parametric Si found already above. The oxide layer is the layer 5 in Table I modeled through the Sellmeier function. Fitting parameter for this layer is the thickness. Figure 6 represents the dielectric functions of all composite layers.

The existence of Ge WL and Ge dot layer implies noticeable absorption for the propagating electromagnetic field in the Si/Ge structure emitted from the dots. This absorption cannot be ignored and can play an important role in photonic devices like that presented in Ref. 32.

To investigate whether the optical resonances in Ge dots can be observed by means of spectroscopic ellipsometry, samples with a stack of Ge dots were also probed. Measurements with a conventional rotating polarizer/analyzer ellipsometer did not reveal any specific feature of the Ge dots due to the insufficient sensitivity of the setup. To probe the stack of Ge dots, we carried out experiments on high sensitivity Bruker Vertex v80 spectrometer with *p*- and *s*-polarized beams. Figure 7 represents the measured value of Ψ at two different angles of incidence—74° and 80°.

An indication of the Ge dots and Ge WL response can be recognized in the spectral range between 0.6 and 0.95 eV.[15] The sharper peak at 1.45 eV can be explained tentatively by the presence of small Ge QDs.[35,36] In Refs. 32 and 33 photoluminescence of small Ge dots (diameter of 1–10 nm) in SiOx and GeOx matrices was reported in the range around 1.4 eV. Figure 1(a) illustrates presence of bigger domelike and smaller pyramidlike Ge dots and we assume that the smaller Ge

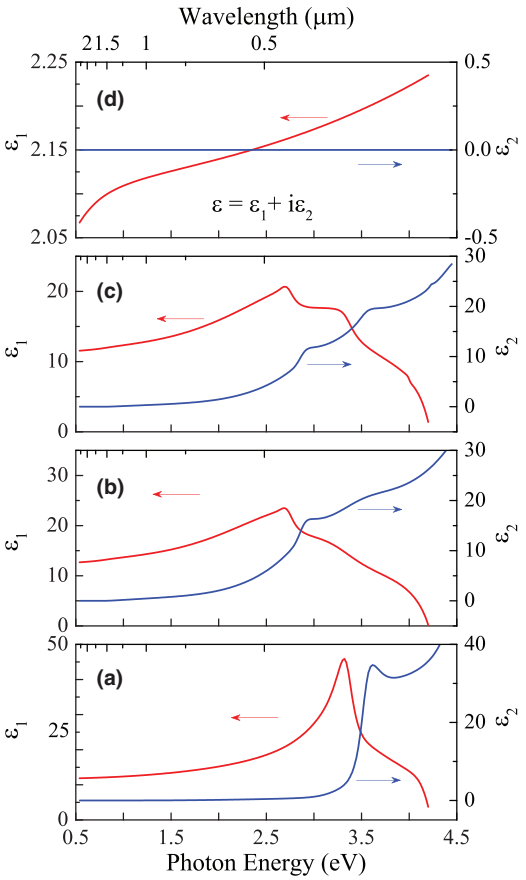

FIG. 6. (Color online) Complex dielectric functions of the sample layers: (a) Si substrate, (b) Ge WL, (c) Ge dots layer, and (d) oxide Si capping. The optical constants of Si buffer and Si capping layers do not differ from those of Si substrate and are not shown here. Note that graph labeling is upward to follow the as grown layer sequence of the samples.

dots may cause the PL at 1.45 eV, though more investigations are needed to study this problem in detail. The model, derived for the one-layer sample above, has been applied to this sample as well (accounting the multiple layers with Ge dots). It can fit the spectral region ∼0.6–1.35 eV, but it is not appropriate for describing the 1.4 eV peak, that is, corresponding modification in the model is required to characterize the peak. The dotted lines in Fig. 7 show the direct application of the model. However, it produces errors surpassing reasonable confidence limits. Fitting the measurements in Fig. 7 would require also a more complex model. It should take into account such facts like (i) change of the dot sizes from layer to layer [see Fig. 1(b)], (ii) change of the Ge WL thickness from layer to layer, (iii) presence of Ge dots with different sizes within a same layer, (iv) presence of Ge dots of ellipsoidal form (i.e., different axes lengths), and (v) nonspherical form of the Ge dots. These modifications can contribute to the further improvement of the model.

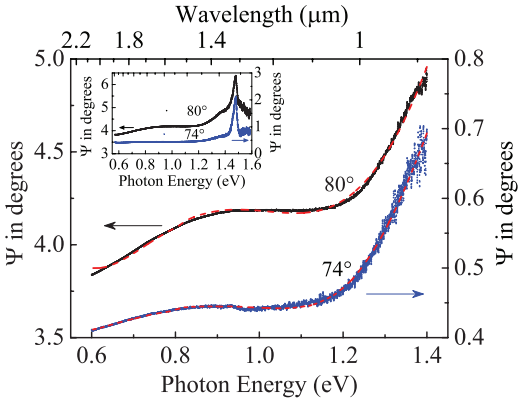

FIG. 7. (Color online) Experimentally measured values for Ψ at 74° and 80° of a stack of Ge dots. Fitting is not shown in this graph.

As it can be seen both from the PL and from the photoresponse spectra in Fig. 5, the Ge dots samples exhibit a broad response in the region approximately from 0.7 to 1 eV. In this regard, the broad feature on the ellipsometry measurement in Fig. 4 in the range 0.65–0.95 eV can be expected and has been intuitively ascribed to the presence of Ge dots and Ge WL. Additional measurements can be performed to prove if the intrinsic doping of the substrate has caused contribution to the 1.4 eV peak or it is purely due to the presence of smaller dots, as we assume.

IV. CONCLUSIONS

In this paper we have presented an investigation of the optical parameters of Si-based multilayer structures containing Ge islands. A theoretical model for describing the ellipsometry measurements on the structures has been introduced. The model introduces an error regarding the thickness of the Ge dot layer. We believe that the main reason behind is the nature of the effective medium approximation. Within this approximation, the Ge dots are treated as spheres with a dielectric function $\varepsilon_{\mathrm{CDA}}$ residing in Si host material. From the TEM and SEM images in Fig. 1, it is clear that the dots have in reality pyramidal and dome shapes, which results in parameter averaging and finally different thickness. Although this fact, our work is an attempt to treat the problem of dielectric function of nanostructures and to give input values for the simulation codes needed for optimization of Si/Ge based devices. The complex refractive index is an important parameter when we consider, for example, the design of an optical waveguide for the electromagnetic field emitted by the Ge islands. The ellipsometry technique, widely utilized by many research groups for different systems, was applied here for QDs by incorporating the islandlike structure of Ge dots in Si matrix also in the model (layer 3 in Table I). The technique allowed determination of the optical constants of all the layers. The global dielectric function is $\tilde{\varepsilon} = 12.134 + i \cdot 0$ giving an effective global refractive index of the structure $\tilde{n} \approx 3.48$–3.49. This is the dielectric function of silicon at $\lambda = 1500$ nm (0.82 eV) increased due to the presence of Ge. All Si layers were found to exhibit $\varepsilon_r = 12.134$ and $\varepsilon_i = 0$ [$\mathrm{Re}(\tilde{n}) = 3.48$ and $\mathrm{Im}(n) = 0$] behaving as bulk Si, whereas the Ge wetting layer has nearly the properties of the bulk Ge with $\varepsilon_r = 18.144$ and $\varepsilon_i = 0.488$ [$\mathrm{Re}(\tilde{n}) = 4.26$,$\mathrm{Im}(n) = 0.057$]. The layer with Ge dots showed $\mathrm{Re}(\tilde{n}) = 3.47$ and $\mathrm{Im}(n) = 0.03$, which means that the refractive index is nearly equal to that of Si due to the high volume fraction of Si in the layer. At the same time, the layer shows absorption nearly equal to that of Ge at the corresponding photon energy. This

information was efficiently used in BPM simulation code for optimization of active waveguides[15] and a waveguide based NIR photodetector.[15] BPM simulations calculate the modes developing in the waveguides and were used for optimization of the WGs dimensions. At the same time, this information can be applied by the photonic community for design and optimization of photonic/optoelectronic devices.

ACKNOWLEDGMENTS

The authors thank the ACCM (Austrian Center of Competence in Mechatronics) and Bernhard Jakoby for the support of this work. We also acknowledge the aid from the PLATON and the IRON projects of the Austrian Nano-initiative. We like to express our gratitude to Friedrich Schäffler for his support in growing the films and for the helpful discussions. Special thanks are given to Pascal Schley and Rüdiger Goldhahn from Institut für Physik, Technische Universität Ilmenau, 98693 Ilmenau, Germany for their support in the ellipsometry experiments and discussions. We assert our appreciation to Blaine Johs and Tom Tiwald from J. A. Woollam Co. for the discussions in our private communication.

APPENDIX A: SHORT INTRODUCTION IN THE THEORY OF PARAMETRIC SEMICONDUCTOR MODEL

The model starts with the following expression for the complex dielectric function:

$$\varepsilon(\hbar\omega) = 1 + i\int_0^\infty S(x)\Phi(\hbar\omega,x)dx.$$

Integration is performed over the energy spectrum and x is the integration variable. $S(E)$ is the unbroadened absorption spectrum. The broadening function Φ is either Lorentzian or Gaussian and will be constructed so that the Kramers-Kronig consistency is included in it:

$$\Phi(\hbar w,E) = \int_0^\infty e^{i[\hbar w - E + i\gamma(s)]s}ds - \int_0^\infty e^{i[\hbar w + E + i\gamma(s)]s}ds,$$

$\gamma(s) = 2\sigma^2 s$ is the Gaussian broadening parameter.

Furthermore, the integration is restricted to the energy range, in which measurements are performed. Then a term is added to account for oscillators describing high energy absorption outside the measured range. The function $S(x) = f(E)$ is broken into pieces with each piece having own constant broadening parameter:

$$\varepsilon(\hbar\omega) = 1 + i\sum_{j=1}^{n}\int_{E_{\min}}^{E_{\max}} S_j(x)\Phi_j(\hbar\omega,x,\sigma_j)dx + \sum_{j=n+1}^{n+P+1}\frac{A_j}{(\hbar\omega)^2 - E_j^2}.$$

This means that each CP has own broadening parameter σ_j at energy E_C as well. In order to evaluate the integral numerically, either δ functions $S_j(E) = \delta(E - E_j)$ or bounded polynomials $S_j(E) = \sum_{k=0}^{N} p_{j,k}E^k u(E - a_j)u(b_j - E) = \sum_{k=0}^{N} p_{j,k}E^k$, $a_j < E < b_j$ must be used.

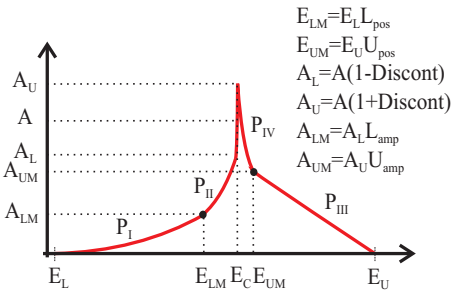

FIG. 8. (Color online) Unbroadened CP structure composed of four component polynomials, $P_{\rm I}$, $P_{\rm II}$, $P_{\rm III}$, and $P_{\rm IV}$.

The polynomials are grouped in ensemble of four and span a bounded spectral region (Fig. 8). The characteristic parameters for each CP are shown in Table II. These parameters determine uniquely polynomials in energy, $P_{\rm I}$, $P_{\rm II}$, $P_{\rm III}$, and $P_{\rm IV}$, which must be joined continuously at the joint points. Since discontinuity of the joint density of states at the CPs is allowed, then discontinuity in amplitude at the center is also possible.

For Gaussian broadening, the line shape function can be written as

$$\Phi_j(\hbar\omega,E,\sigma_j) = \sqrt{\frac{\pi}{8\sigma^2}}\left[e^{-y_1^2} + e^{-y_1^2}erf\,(iy_1) - e^{-y_2^2} - e^{-y_2^2}erf\,(iy_2)\right],$$

where $y_1 = \frac{\hbar\omega - E}{2\sqrt{2}\sigma}$, $y_2 = \frac{\hbar\omega + E}{2\sqrt{2}\sigma}$.

This can be expressed in terms of $\Phi\prime$: $\Phi_j(\hbar\omega,E,\sigma_j) = \sqrt{\frac{\pi}{8\sigma_j^2}}[\Phi'_j(y_1) - \Phi'_j(y_2)]$.

However, the line shape function must be used in terms of normalized units in order to be able to create a lookup table for the calculations.

Each CP structure can contribute up to four polynomials to the absorption spectra. Next the polynomials in energy are converted to polynomials in normalized energy units:

$$\Sigma_j^+(y) = \sum_{k=0}^{N} p_{j,k}(-2\sqrt{2}\sigma_j y + \hbar\omega)^k = \sum_{k=0}^{N} q_{j,k}^+ y^k,$$
$$y = \frac{\hbar\omega - E}{2\sqrt{2}\sigma},$$
$$\Sigma_j^-(y) = \sum_{k=0}^{N} p_{j,k}(2\sqrt{2}\sigma_j y - \hbar\omega)^k = \sum_{k=0}^{N} q_{j,k}^- y^k,$$
$$y = \frac{\hbar\omega + E}{2\sqrt{2}\sigma}.$$

For evaluation the expression $y^k\Phi'(y)$ within the integral, the following approximation is used:

$$e^{-y^2}\mathrm{erf}(iy) \approx i\left[\frac{y}{\pi} + \frac{2}{\pi}\sum_{m=1}^{\infty}\frac{e^{-m^2/4}}{m}\sinh(my)\right] = \frac{i}{\pi}\left(ye^{-y^2} + \sum_{m=1}^{\infty}\frac{e^{-y^2+my-\frac{m^2}{4}}}{m} - \frac{e^{-y^2-my-\frac{m^2}{4}}}{m}\right).$$

Then a function is introduced and evaluated numerically for $n = 0.4$:

$$\varphi_m(x) = \int_0^x y^m \Phi'(y) dy.$$

The polynomial coefficients q are the solution of a set of four ($N = 4$) equations. Using n polynomials and p δ functions (amplitude A_j) the dielectric function can be written as

$$\varepsilon(\hbar\omega) = 1 + i \sum_{j=1}^{n} \int_{a_j}^{b_j} S_j(x) \Phi\left(\hbar\omega, x, \sigma_j\right) dx + i \sum_{j=n+1}^{p} A_j \Phi(\hbar\omega, E_j, \sigma_j),$$

which becomes

$$\varepsilon(\hbar\omega) = 1 + i \sum_{j=1}^{n} \sum_{k=0}^{N} q_{j,k}^{+} \left[\varphi_k\left(\frac{\hbar\omega - b_j}{2\sqrt{2}\sigma_j}\right) - \varphi_k\left(\frac{\hbar\omega - a_j}{2\sqrt{2}\sigma_j}\right) \right] - q_{j,k}^{-} \left[\varphi_k\left(\frac{\hbar\omega + b_j}{2\sqrt{2}\sigma_j}\right) - \varphi_k\left(\frac{\hbar\omega + a_j}{2\sqrt{2}\sigma_j}\right) \right]$$
$$+ i \sum_{j=n+1}^{p} A_j \left[\Phi'\left(\frac{\hbar\omega - E_j}{2\sqrt{2}\sigma_j}\right) - \Phi\prime\left(\frac{\hbar\omega + E_j}{2\sqrt{2}\sigma_j}\right) \right].$$

The component polynomials for each CP structure are defined as functions of energy using the following normalized variables:

$$y_{\mathrm{I}} = \frac{E - E_L}{E_{LM} - E_L}, \quad y_{\mathrm{II}} = \frac{E - E_{LM}}{E_C - E_{LM}}, \quad y_{\mathrm{III}} = \frac{E_U - E}{E_U - E_{UM}}, \quad \text{and} \quad y_{\mathrm{IV}} = \frac{E_{UM} - E}{E_{UM} - E_C}.$$

The definition of the polynomials is

$$P_{\mathrm{I}} = A_{LM} \left[(1 - L_{2\mathrm{nd}}) y_I + L_{2\mathrm{nd}} y_I^2 \right] u(E - E_L)\, u(E_{LM} - E),$$

$$P_{\mathrm{III}} = A_{UM} \left[(1 - U_{2\mathrm{nd}}) y_{III} + U_{2\mathrm{nd}} y_{III}^2 \right] u(E - E_{UM})\, u(E_U - E),$$

$$P_{\mathrm{II}} = \left\{ A_{LM} + (1 - A_{LM}) \left[(1 - c_L - d_L) y_{\mathrm{II}} + c_L y_{\mathrm{II}}^2 + d_L y_{\mathrm{II}}^4 \right] \right\} u(E - E_{LM})\, u(E_C - E),$$

$$P_{\mathrm{IV}} = \left\{ A_{UM} + (1 - A_{UM}) \left[(1 - c_U - d_U) y_{\mathrm{IV}} + c_U y_{\mathrm{IV}}^2 + d_U y_{\mathrm{IV}}^4 \right] \right\} u(E - E_C)\, u(E_{UM} - E),$$

where

$$c_L = L_{2\mathrm{nd}} \frac{A_{LM}}{1 - A_{LM}} \left(\frac{E_{\mathrm{C}} - E_{LM}}{E_{LM} - E_L} \right)^2 \quad \text{and} \quad d_L = \frac{1}{1 - A_{LM}} \left[1 - \frac{E_C - E_{LM}}{E_{LM} - E_L} A_{LM} (E_C - E_L) \left(\frac{L_{2\mathrm{nd}}}{E_{LM} - E_L} + \frac{1}{E_C - E_{LM}} \right) \right].$$

For each $-1 < L_{2\mathrm{nd}}(U_{2\mathrm{nd}}) < 1$ the component polynomials will be purely positive.

APPENDIX B

The interpretation and understanding of the measurements of Fig. 7 can start with a Lorentzian fit of the measurement (Fig. 9). We fitted the ellipsometry measurement of Fig. 7 for $\Psi = 80^\circ$ (where the response of the Ge dots and the Ge WL is seen stronger) with four Lorentzian oscillators.

The lowest energy peak is positioned at energy $E_1 = 0.94$ eV, the next are at $E_2 = 1.43$ eV, $E_3 = 1.48$ eV, and $E_4 = 1.56$ eV. The peak E_1 is the broadest one with a FWHM = 0.35 eV. The peak E_3 is approximately in the middle between the peaks E_2 and E_4, which form something like shoulders in the accumulative peak (dashed line). However, deeper discussion of this measurement will not be introduced here until we modify the model and apply it to this measurement. Thus, we also like to elude incorrect interpretations by the readers. Our purpose is, of course, not to use simply Lorentzians for fitting the results in Fig. 7 but to implement successfully the developed model to this measurement and discuss the origin of the features on it.

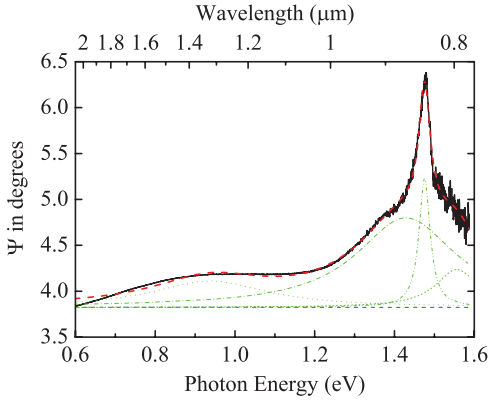

FIG. 9. (Color online) Lorentzian fit of the measurements of Fig. 7 for $\Psi = 80^\circ$ by four oscillators. The dashed line represents the cumulative curve.

*Corresponding authors: gang.chen@jku.at; ventsislav.lavchiev@jku.at

[1]G. Medeiros-Ribeiro, A. M. Bratkovski, T. I. Kamins, D. A. A. Ohlberg, and R. S. Williams, Science **279**, 353 (1998).
[2]J. V. Barth, G. Constantini, and K. Kern, Nature (London) **437**, 671 (2005).
[3]A. Rastelli, M. Stoffel, J. Tersoff, G. S. Kar, and O. G. Schmidt, Phys. Rev. Lett. **95**, 026103 (2005).
[4]Edited by O. G. Schmidt, *Lateral Alignment of Epitaxial Quantum Dots* (Springer, Berlin, 2007).
[5]I. Goldfarb, P. T. Hayden, J. H. G. Owen, and G. A. D. Briggs, Phys. Rev. B **56**, 10459 (1997).
[6]F. M. Ross, J. Tersoff, and R.M. Tromp, Phys. Rev. Lett. **80**, 984 (1998).
[7]Z. Zhong and G. Bauer, Appl. Phys. Lett. **84**, 1922 (2009).
[8]G. Chen, H. Lichtenberger, G. Bauer, W. Jantsch, and F. Schäffler, Phys. Rev. B **74**, 035302 (2006).
[9]G. Chen, G. Vastola1, H. Lichtenberger, D. Pachinger, G. Bauer, W. Jantsch, F. Schäffler, and L. Miglio, Appl. Phys. Lett. **92**, 113106 (2008).
[10]F. M. Ross, R. M. Tromp, and M. C. Reuter, Science **286**, 1931 (1999).
[11]A. Rastelli, M. Stoffel, J. Tersoff, G. S. Kar, and O. G. Schmidt, Phys. Rev. Lett. **95**, 026103 (2005).
[12]O. E. Shklyaev, M. J. Beck, M. Asta, M. J. Miksis, and P. W. Voorhees, Phys. Rev. Lett. **94**, 176102 (2005).
[13]J. Liu *et al.*, Appl. Phys. Lett. **87**, 103501 (2005).
[14]H. Presting, J. Konlea, H. Kibbela, and F. Banhartb, Physica E **14**, 249 (2002).
[15]V. Lavchiev, R. Holly, G. Chen, F. Schäffler, R. Goldhahn, and W. Jantsch, Opt. Lett. **34**, 3785 (2009).
[16]M. Brehm, M. Grydlik, F. Hackl, E. Lausecker, T. Fromherz, and G. Bauer, Nanoscale Res. Lett. **5**, 1868 (2010).
[17]O. G. Schmidt and K. Eberl, IEEE Trans. Electron Devices **48**, 1175 (2001).
[18]G. S. Kar, S. Kiravittaya, U. Denker, B.-Y. Nguyen, and O. G. Schmidt, Appl. Phys. Lett. **88**, 253108 (2006).
[19]E. Kasper and D. J. Paul, *Silicon Quantum Integrated Circuits*, Springer Series on NanoScience and Technology (Springer, Berlin, 2005).
[20]D. Grützmacher, C. Dais, L. Zhang, E. Müller, and H. K. Solak, Mater. Sci. Eng. C-biomimetic Supramolecular Syst. **27**, Special Issue, 947 (2007).
[21]R. Ichikawa, S. Takita, Y. Ishikawa, and K. Wada, Top. Appl. Phys. **119**, 131 (2011).
[22]P. Boucaud *et al.*, Thin Solid Films **517**, 121 (2008).
[23]J. S. Xia, Y. Ikegami, Y. Shiraki, N. Usami, and Y. Nakata, Appl. Phys. Lett. **89**, 201102 (2006).
[24]J. S. Xia, K. Nemoto, Y. Ikegami, and Y. Shiraki, Appl. Phys. Lett. **91**, 011104 (2007).
[25]J. S. Xia, Y. Takeda, N. Usami, T. Maruizumi, and Y. Shiraki, Opt. Express **18**, 13945 (2010).
[26]W. H. Press, B. P. Flannery, S. A. Teukolsky, and W. T. Vetterling, *Numerical Recipes in C* (Cambridge University Press, Cambridge, 1988).
[27]G. E. Jelisson, Jr., Thin Solid Films **33**, 313 (1998).
[28]B. Gallas and J. Rivory, J. Appl. Phys. **94**, 2248 (2003).
[29]D. V. Marin, E. B. Gorokhov, A. G. Borisov, and V. A. Volodin, Opt. Spectrosc. **106**, 436 (2009).
[30]Y. Ogawa, F. Minami, Y. Abate, and S. R. Leone, Appl. Phys. Lett. **96**, 063107 (2010).
[31]www.rsoftgroup.com.
[32]V. Lavchiev, G. Chen, and W. Jantsch, Thin Solid Films **518**, 2573 (2010).
[33]C. M. Herzinger and B. Johs (unpublished).
[34]D. E. Aspnes, Thin Solid Films **89**, 249 (1982).
[35]E. B. Kaganovich, E. G. Manoilov, and E. V. Begun, Semiconductors **41**, 172 (2007).
[36]E. B. Kaganovich, D. V. Korbatyak, Yu. V. Kryuchenko, I. M. Kupchak, E. G. Manoilov, and A. V. Sachenko, Nanotechnology **18**, 295401 (2007).